Standardization of post-mortem photoelectron spectroscopy studies of battery interphases: from cell assembly to data analysis

Downloaded from: https://research.chalmers.se, 2026-06-30 16:19 UTC

Citation for the original published paper (version of record):
Herrera, C., Capone, F., Fantin, R. et al (2026). Standardization of post-mortem photoelectron spectroscopy studies of battery interphases: from
cell assembly to data analysis. Journal of Energy Storage, 170.
http://dx.doi.org/10.1016/j.est.2026.122820

N.B. When citing this work, cite the original published paper.

research.chalmers.se offers the possibility of retrieving research publications produced at Chalmers University of Technology. It covers all kind of research output: articles, dissertations, conference papers, reports etc. since 2004. research.chalmers.se is administrated and maintained by Chalmers Library

(article starts on next page)

Journal of Energy Storage 170 (2026) 122820

Contents lists available at ScienceDirect

Journal of Energy Storage

journal homepage: www.elsevier.com/locate/est

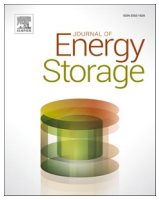

Research papers

Standardization of post-mortem photoelectron spectroscopy studies of battery interphases: from cell assembly to data analysis

Cinthya N. Herrera [a,b,*], Federico Capone [c], Roberto Fantin [d,e], François Cadiou [f], Nataliia Mozhzhukhina [g,p], Quentin Jacquet [h], Jackson Flowers [i], Stefan Fuchs [i], Kristina Edström [j], Andrew Naylor [j], Lucía Pérez Ramírez [c], Alexandre Ponrouch [k], Deyana S. Tchitchekova [k], Giorgio Baraldi [l], Elixabete Ayerbe [m], Christian Wölke [n], Isidora Cekic-Laskovic [n], Martin Winter [n], Khawla Zrikem [e], Shatakshi Saxena [e], Thanh-Loan Lai [e], Jean-Pascal Rueff [c], Poul Norby [o], Sandrine Lyonnard [h,*], Anass Benayad [d,e,q,**]

[a] Institut Laue-Langevin, 71 av. de Martyrs, 38000, Grenoble, France
[b] Université Grenoble Alpes, CEA, IRIG-MEM-L_SIM, 17 avenue des Martyrs, 38000, Grenoble, France
[c] Synchrotron SOLEIL, L'Orme des Merisiers, 91190, Saint-Aubin, France
[d] Université Grenoble Alpes, F-38000, Grenoble, France
[e] CEA-LITEN-DTNM, F-38054, Grenoble, France
[f] ESRF, 71 av. de Martyrs, 38000, Grenoble, France
[g] Department of Physics, Chalmers University of Technology, 412 96, Göteborg, Sweden
[h] Université Grenoble Alpes, CEA, CNRS, Grenoble INP, IRIG, SyMMES, 17 avenue des Martyrs, 38000, Grenoble, France
[i] Karlsruhe Institute of Technology (KIT) Institute of Physical Chemistry (IPC)Fritz-Haber-Weg 2, 76131, Karlsruhe, Germany
[j] Department of Chemistry – Ångström, LaboratoryUppsala University, Box 538, Uppsala, S-751 21, Sweden
[k] Institut de Ciència de Materials de Barcelona, ICMAB-CSIC, Campus UAB, Bellaterra, 08193, Spain
[l] Centre for Cooperative Research on Alternative Energies (CIC energiGUNE), Basque Researchand Technology Alliance (BRTA), 01510, Vitoria-Gasteiz, Spain
[m] CIDETEC, Basque Research and Technology Alliance (BRTA), Spain
[n] Helmholtz-Institute Münster (IMD4), Forschungszentrum Münster, Corrensstraße 48, 48149, Münster, Germany
[o] Department of Energy Conversion and Storage, Technical University of Denmark, 2800, Kgs. Lyngby, Denmark
[p] SEEL Swedish Electric Transport Laboratory, Säve Flygplatsväg 27, 42373, Gothenburg, Sweden
[q] Institute for Applied Materials (IAM), Karlsruhe Institute of Technology (KIT), 76344, Eggenstein-Leopoldshafen, Germany

ARTICLE INFO

Keywords:
Post-mortem
XPS
SEI
Round-robin

ABSTRACT

Understanding the chemical structure of the solid electrolyte interphase that forms and evolves during lithium-ion battery cycling is critical for advancing battery technology. This complex task often requires the use of post-mortem protocols to extract the electrodes in controlled states of charge and prepare them for further characterization and analysis. Over decades of research and optimization, the scientific community has established and shared post-mortem workflow protocols tailored to specific techniques. However, numerous sources of artifacts can disturb this workflow, introducing experimental uncertainties at various stages, from electrode manufacturing to data interpretation. Here we present the results of a round-robin inter-laboratory study using post-mortem X-ray photoemission spectroscopy to characterize the solid electrolyte interphase formed on graphite electrode after cycling in two different electrolytes. Several leading European research teams, expert in battery manufacturing and characterization by X-ray photoemission spectroscopy, participated in a meticulously designed post-mortem workflow. The goal was to identify the sources of consistency and disparity in the results and their impact on the scientific conclusions. Moreover, human-induced bias and errors were quantified throughout key steps, from cell assembly to photoemission core level peak fitting and interpretation. Based on our findings, we offer key recommendations for identifying and minimizing sources of artifacts in the analysis of

* Corresponding authors.
** Corresponding author at: Université Grenoble Alpes, F-38000, Grenoble, France.
E-mail addresses: Cinthya.HERRERACONTRERAS@cea.fr (C.N. Herrera), sandrine.lyonnard@cea.fr (S. Lyonnard), anass.benayad@kit.edu (A. Benayad).

https://doi.org/10.1016/j.est.2026.122820
Received 18 September 2025; Received in revised form 2 April 2026; Accepted 19 May 2026
Available online 28 May 2026
2352-152X/© 2026 The Authors. Published by Elsevier Ltd. This is an open access article under the CC BY license (http://creativecommons.org/licenses/by/4.0/).

the solid electrolyte interphase chemical composition. Effectively addressing these challenges is essential for improving both the performance and longevity of batteries.

1. Introduction

Improving lithium-ion battery (LIB) performance requires a fundamental understanding of the electrochemical mechanisms occurring during cell operation to bring optimal solutions with higher safety and efficiency requirement. The solid electrolyte interphase (SEI), a heterogeneous ionically conducting and electronically insulating layer, forms at the interface between the negative electrode and electrolyte during electrochemical cycling and plays a key role in LIB function and performances retention [1]. It acts as a protective layer towards active material degradation but also evolves dynamically during the cycle life of a battery, leading to performances fading.

Designing stable SEIs has thus become a major research focus for mitigating aging and enhancing the lifetime of LIBs. Many studies have investigated the chemical composition and distribution of species in the SEI via advanced physico-chemical characterizations of the electrode surface. As a result, many phenomenological models were initially proposed, from a single ionic conductive layer [1] to a double-layered structure composed of a thin compact layer adjacent to the electrode and a thick, porous layer near the electrolyte [1–3]. Subsequent studies on the SEI properties led to the currently widely accepted phenomenological mosaic model, which describes the SEI as a complex assembly of multiple organic and inorganic domains [4–9].

For graphite electrodes cycled in a common carbonate ester-based electrolyte with lithium hexafluorophosphates salt ($LiPF_6$), the SEI typically contains inorganic lithium compounds such as alkyl lithium carbonates or lithium carbonates (ROCOOLi, Li_2CO_3), phosphate groups (POF_X), and lithium fluoride (LiF) [6,7,10–12]. However, accurately resolving the SEI's composition, thickness, and structural evolution, which are highly dependent on numerous parameters [13], remains a significant challenge. Its chemical complexity and sensitivity to air have made it difficult to unambiguously define the nature and role of individual species, often leading to conflicting interpretations in the literature.

Most of the SEI models are constructed based on experimental post-mortem analysis involving surface and/or spectroscopic characterization techniques [14,15], which are powerful for studying battery materials and interphases. The SEI's chemical composition has been extensively scrutinized by X-ray photoelectron spectroscopy (XPS) [16–18], Fourier-transform infrared spectroscopy (FTIR) [19], Raman and Auger spectroscopies (AES) [20–22], and Nuclear Magnetic Resonance (NMR) [23,24]. Among these, XPS stands out as a non-destructive technique, offering deep insight into the SEI composition by revealing the surface chemical bonding of the SEI and providing semi-quantitative analysis [25,26].

However, the characterization of such a thin and chemically complex layer necessitates suitable protocols, from sample preparation to data interpretation. Every step in the post-mortem analysis workflow – including cell assembly and cycling, cell opening, electrode preparation for physico-chemical characterization, sample transfer from argon-filled glove boxes to characterization tools, experimental setup for data acquisition and data analysis - constitutes a potential source of artifacts [27–30]. Human factors, including the level of expertise at each step of the workflow or reproducibility among different operators, introduce additional sources of bias and errors. The absence of standardized procedures across laboratories thus remains a major limitation.

To ensure more reliable SEI investigations and enable meaningful comparison between studies, it is crucial to address these uncertainties and establish reproducible, standardized experimental protocols.

Large-scale initiatives are necessary to establish standardization in the community and tackle the reproducibility issue of cell preparation and testing [31–33], post-mortem interfaces investigations [34] or *operando* synchrotron studies [35]. One major goal is to generate high fidelity quality-assessed data through robust acquisition and analysis pipelines widely adopted by researchers and insuring reproducibility according to selected criteria. Along this line, the Battery Interface Genome Materials Acceleration Platform (BIG-MAP) project, developed under the umbrella of the European large-scale initiative Battery 2030+, set the foundations of standardized workflows for accelerating battery discovery, based on an artificial intelligence (AI)-centric infrastructure using ontologized tools and embedding multi-techniques characterizations [36–38].

Within this framework, we evaluated and quantified the level of uncertainty associated with each step of post-mortem XPS workflows applied to the analysis of SEI composition on the surface of cycled graphite electrodes. Our focus was on identifying sources of variability introduced during cell assembly, sample preparation, XPS data acquisition, and subsequent data analysis and interpretation. We critically assessed the biases introduced at each step of the process, examined the impact of human and instrumental factors, and proposed recommendations to minimize artifacts and enhance reproducibility. To this end, we implemented a methodology based on two inter-laboratory workflows, whose detailed designs are described in the following section. Our findings provide insights that extend beyond XPS, offering guidance for other characterization techniques where similar sources of uncertainties and deviations are encountered.

2. Experimental multi-partner XPS workflow

To assess the quality and reproducibility of post-mortem SEI characterization and analysis using XPS, we implemented two sequential inter-laboratory workflows. The first was a **blind reproducibility study**, designed to assess the reproducibility of results by identifying potential sources of artifacts arising from cell assembly, post-mortem sample preparation, and XPS acquisition. Based on insights gained from this study, a subsequent **standardized workflow** was developed incorporating standardized experimental protocols to minimize procedural variability. This standardized workflow included a round-robin data analysis exercise to address potential interpretative biases, thus extending the standardization effort to the data analysis stage. Both workflows followed a similar structure from cell assembly to data interpretation, allowing for a systematic comparison and refinement of experimental practices. The combination of standardized experimental protocols with collaborative data analysis forms the basis for a fully standardized and reproducible workflow that integrates optimized procedures across all stages. These two sequenced workflows are schematically represented in Fig. 1 and described in detail below.

2.1. Sample preparation and handling

The cell assembly and cycling procedures were common to both workflows and are illustrated in the top-left panel of Fig. 1. Coin cells were assembled following the BIG-MAP standard protocol [39], using graphite, manufactured by CIDETEC, as the negative electrode and $LiNiO_2$, manufactured by BASF, as the positive electrode. Coin cells were filled with LP57 electrolyte with and without additives according to three formulations:

- 1 m $LiPF_6$ in ethylene carbonate- ethyl methyl carbonate (EC:EMC) (3:7), used for the blind reproducibility study, and
- 1 m $LiPF_6$ in EC:EMC (3:7) + 2 wt% vinylene carbonate (VC) and

- 0.95 m $LiPF_6$ + 0.05 m LiTDI (Lithium 4,5-dicyano-2-trifluoromethylimidazole) in EC:EMC (3:7) + 2 wt% VC, used for the standardized workflow.

The electrochemical cycling protocol consisted of an initial formation step, a series of diagnostic check-ups, and repeated accelerated aging cycles. Cells were first subjected to a 6 h open-circuit voltage (OCV) rest, followed by three galvanostatic formation cycles at C/10, each comprising a constant-current (CC) charge at C/10 with a constant-voltage (CV) hold to a cut-off of I < C/20, and a CC discharge at C/10. An initial check-up cycle was then performed using a CC charge/discharge at C/20 followed by a CV step with a cut-off of I < C/50 in both directions, providing the beginning-of-life (BoL) discharge specific capacity. Accelerated aging was induced by applying sets of 20 galvanostatic cycles consisting of a CC–CV charge at 1C (CV cut-off I < C/20) and a CC discharge at 1C. After each aging block, a follow-up check-up identical to the initial diagnostic cycle was conducted to obtain the current discharge specific capacity and calculate the state of health (SoH). Steps of aging and check-up were repeated until the SoH dropped to ≤80%, which was considered the end of life (EoL) of the cell. All tests were performed within a voltage window of 2.5–4.2 V at 20 °C in temperature-controlled cycling chambers, with the 1C current defined from the active material mass and a practical specific capacity of 225 mAh g^{-1}. All electrochemical protocols are listed in Table 1.

After cycling, cells were dismantled in an argon-filled glove box (H_2O, O_2 < 0.5 ppm), and electrodes were rinsed in EMC and sealed in airtight pouch cells and shipped to the XPS laboratories listed in Table 2. All details related to washing process are listed in Table 1.

Each laboratory stored samples in an argon-filled glove box and used airtight transfer vessels to transport them to the XPS instrument. Partners performed XPS acquisition based on their in-house post-mortem protocols. These steps are outlined in the middle-top panel of Fig. 1.

While the overall structure of both workflows remained consistent, slight differences in cell assembly were applied. The specifications for each are detailed below:

1. **Blind reproducibility study**: Two full LNO/Graphite coin cells with identical components were assembled and cycled by two partner institutions using the standard LP57 electrolyte formulation and the cycling protocol described previously. The cells are named Cell 1 and 2 in the following manuscript. After cycling and cells dismantling, the graphite electrodes were cut in two or three sections and sent to multiple XPS laboratories. Before XPS measurements, the electrodes were washed twice for one minute in dimethyl carbonates (DMC) to remove residual salt.

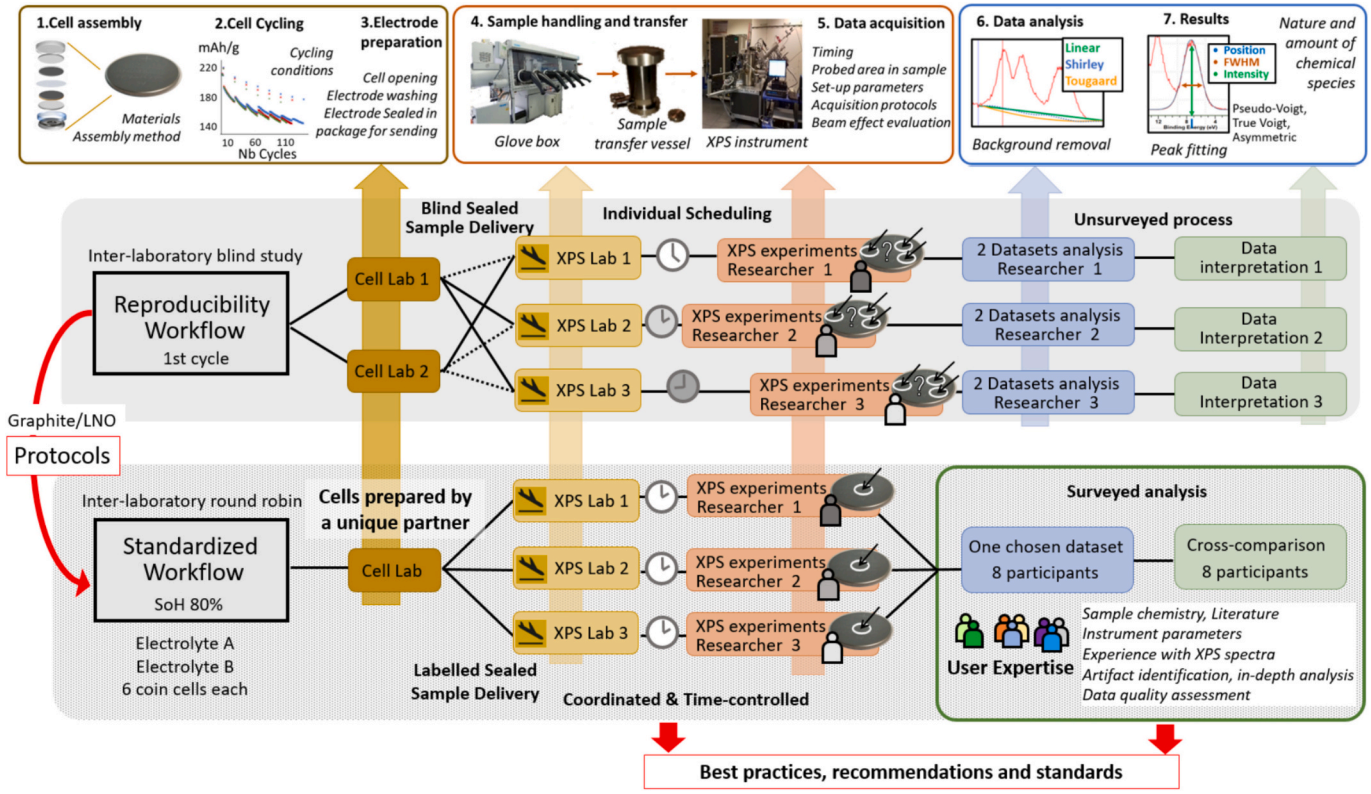

Fig. 1. Schematic overview of the two inter-laboratory workflows. The three top panels illustrate the shared structure of both workflows, covering the entire process from cell assembly to data interpretation. The left panel details electrode and cell preparation, including cell components, cycling protocols and post-mortem handling (opening, washing, sealing). The central panel represents the instrumental setup for sample transfer and XPS measurement (e.g. glove box, transfer vessels), and highlights five critical parameters influencing data quality: acquisition timing, probe area location, instrument settings, measurement protocols, and beam-induced effects. The right panel outlines the data processing stages: background subtraction, peak fitting, and SEI species quantification. The bottom section illustrates the implementation of the two workflows. In the blind reproducibility study, two partners independently assembled and cycled cells, to finally shipped them to multiple XPS laboratories. They subsequently characterized the samples without centralized coordination. Measurements were taken at unspecified positions on the surface of the electrode and at unspecified schedules. Each XPS partner performed independent data analysis, and results were later compared. This reproducibility study enabled the definition of harmonized protocols for cell assembly, preparation, and data acquisition, targeting the minimization of artifacts, which directly served as the foundation for the standardized workflow. In the standardized workflow, a single partner prepared all cells, XPS partners followed defined acquisition protocols. Measurements were time- and location- constrained (central electrode region), and a round-robin analysis was conducted using datasets from a single laboratory. This enabled the establishment of robust and reproducible analysis procedures. Together, both workflows underpin the recommended best practices for post-mortem XPS analysis of battery electrodes and highlight the importance of standardization in inter-laboratory studies.

Table 1
Experimental protocols for sample preparation. Standardized Electrochemical cycling (aging) and standardized XPS sample preparation after EoL.

Protocol	Step	Name	Voltage range	1C current	Temperature	Environment	Operation			Additional data	SoH
Electrochemical cycling (aging)			2.5 to 4.2 V	Active material mass + practical capacity of 225mAh/g	20 °C	Coin cell (CR2032)	6h rest			OCV	-
	1	Formation					3x	Charge	CC	C/10	-
									CV	Cut-off I < C/20	
								Discharge	CC	C/10	
	2	Check-up cycle					1x	Charge	CC	C/20	Initial specific discharge capacity ($D_{c,init}$) for SoH = 100%
									CV	Cut-off I < C/50	
								Discharge	CC	C/20	
									CV	Cut-C/50	
	3	Aging					20x	Charge	CC	1C	-
									CV	Cut-off I < C/20	
								Discharge	CC	1C	
	4	Check-up					see step 2			see step 2	Current specific discharge capacity ($D_{c,curr}$) SoH = $D_{c,curr}$/ $D_{c,init}$
	5	Repeat cycling					Repeat steps 3 & 4			Until SoH ≤ 80% at the end of step 4 repeat	-
XPS sample preparation	a	Cell disassembly	-	-	-	Glovebox	As soon as possible			Ar atmosphere O_2 level ≤ 0.1 ppm H_2O level ≤ 0.5 ppm	-
	b	Soak					30s, 1mL EMC				
	c	Decanting					-				
	d	Soak					See step b				
	e	Packaging					Sealed in Al-laminated bags				

Table 2
Details on partners performing the XPS characterization.

	Partner 1	Partner 2	Partner 3
XPS type	Lab-based XPS	Lab-based XPS	Synchrotron HAXPES
Institution	CEA	Uppsala University (UU)	SOLEIL GALAXIES beamline
X-ray energy	1486 eV (Al Kα) QUANTES/ULVAC-PHI. Monochromatised	1486 eV (Al Kα) Kratos AXIS Supra+ Monochromatised	3 KeV / 7 KeV Monochromatised
Take off angle	45°	45°	10°
Beam diameter	200 × 200 μm^2	700 × 300 μm^2	30 × 80 μm^2
Total exposure	Survey spectra: 11 min. *F* 1s (9 min), O 1 s (9 min), N 1 s (16 min), S 2p (16 min), P 2p (19 min), C 1s (9 min), Li 1 s (24 min)	Survey spectra: 2 min. C 1s (75 s), *F* 1s (100–250 s), P 2p (14 min 20 s)	Survey spectra: 3 min
Flux/beam power	7 × 10^9 ph/s (47.8 W)	Al (225 W)	10^{13} ph/s
Resolution	1.6 eV for survey 0.7 eV for core level, estimated based on FWHM (Ag $3d_{5/2}$)	Al Kα optimal energy resolution: 0.48 eV estimated based on FWHM (Ag $3d_{5/2}$)	0.3 eV
Pass energy	224 eV for survey 55 eV for core level	160 eV for survey, 20 eV for core level	200 eV
Peak calibration	C 1s (Graphite C=C at 284 eV or C-C at 285 eV)	C 1s (Graphite C=C at 284 eV or C-C at 285 eV)	C 1s (Graphite C=C at 284 eV or C-C at 285 eV)
Charge neutralization	Off (to avoid beam damage due to charge neutralization)	On (electron only): Current: 0.4 A, Bias: 0.17 V, Charge balance: 0.67 V	Off (to avoid beam damage due to charge neutralization)

2. **Standardized workflow:** Cell assembly and cycling were performed by a single partner with expertise in large-scale cell production. Six cells were prepared, three with standard electrolyte formulation containing VC and three with the same formulation plus LiTDI as an additive. The cells were cycled until reaching a state-of-health (SoH) of 80%. After cell dismantling in argon-filled glove box, graphite electrodes were immediately washed twice for one minute in DMC, dried and sealed in airtight pouch cell, and shipped to partners for XPS acquisition.

2.2. Data acquisition and analysis

The top-right panel in Fig. 1 outlines data analysis, including background removal and peak fitting, and interpretation. While the same analytical technique was used in both workflows, the approach to acquisition and data interpretation differed significantly.

1. **Blind reproducibility study**: Partners performed XPS measurements without centralized coordination, there were no specific guidelines on experimental parameters, or acquisitions strategies or timing. Measurements were conducted at unspecified positions on the electrodes surface. Each laboratory performed acquisitions within four to six weeks after receiving the cycled cells. Each laboratory independently conducted data analysis using CasaXPS software [40], followed by a collective comparison of the results. Acquisition parameters are summarized in Table 2.

2. **Standardized workflow:** XPS acquisition was coordinated across laboratories. Two mandatory guidelines for data acquisition were introduced, (i) measurements had to be conducted within a few days after sample arrival, and (ii) the probed area had to be located in the center of the coin cell. All acquisitions were completed within two weeks from the date of receiving the electrodes. Data analysis and interpretation were conducted through a round-robin inter-laboratory exercise, that adhered to the following protocols:

- The exercise was conducted in person with a panel of eight early-career researchers. While all participants had experience in XPS peak fitting, their expertise in battery materials science varied—only one participant lacked in-depth knowledge in both areas.
- Each participant analyzed the same data set, using CasaXPS software, aided by resources such as several databases, relevant literature [12,16,41] on the SEI analyzed by XPS and the XPS equipment handbooks [42].

3. Results and discussion

To evaluate the impact of the various procedures, from sample preparation to data acquisition and analysis, on the accuracy and reliability of XPS results, we examine the XPS datasets obtained from graphite electrodes obtained through the two inter-laboratory workflows. We first present and discuss the outcomes of the blind reproducibility study, followed by the results of the standardized round-robin workflow focused on standardizing data analysis procedures.

3.1. Reproducibility based on inter-laboratory blind study

The survey spectra acquired during the blind reproducibility study by Partners 1, 2 and 3 (see Table 2) for the two graphite electrode samples are shown in Fig. 2. In all cases, the spectra show the characteristic core-level peaks of graphite electrodes cycled in standard electrolyte, including *F* 1s (and related F KLL Auger transitions), O 1s (and related O KLL Auger transitions), C 1s, N 1s, P 2p, P 2s and Li 1s. Partner 3 measured only one cell. In the spectrum recorded by Partner 3, Auger transitions are not visible due the conservation of the kinetic energy of Auger electron, as consequence of using a 3 keV synchrotron X-ray beam. Notably, differences in carbon and fluorine peak intensities are observed, even though cells 1 and 2 were nominally assembled and cycled under identical conditions. The washing and aging process following cell disassembling may contribute to the observed disparities in the XPS results.

Fig. 3 and Fig. 4 present high-resolution spectra of the C 1s and F 1s core levels, respectively, recorded by Partners 1 and 2 on graphite electrodes from cells 1 and 2, grouped for direct comparison. High-resolution spectra from Partner 3 are not shown, as the greater probing depth with 3 keV X-ray energy is about 15 nm makes the direct comparison with those obtained using Al Kα X-ray in laboratory-based XPS systems (probing depth ~ 5 nm) not straightforward [43]. Spectra acquired on the graphite electrode from Cell 1 were calibrated to the C 1s core level at 285 eV (Fig. 3-a), corresponding to graphitic carbon (a mix of sp^2 and sp^3 related carbon). The *F* 1s peak is centered at 685 eV, indicative of LiF species (see Fig. 4-a), consistent with literature [17]. Calibration to either the aliphatic or graphitic *C* 1s peak is commonly used to accurately determine peak positions relevant to SEI composition. In this case, the spectra from both partners show similar shape. They present a small shoulder at 283 eV and two bands between 285 and 289 eV, assigned to the de-intercalated lithium in the graphite electrode (Li-C) and C-C, C-O, O-C=O, and CO_3 bonds, respectively [18,44].

Note that each partner used different pass-energies to acquire the high-resolution spectra. This parameter has an impact on the spectra

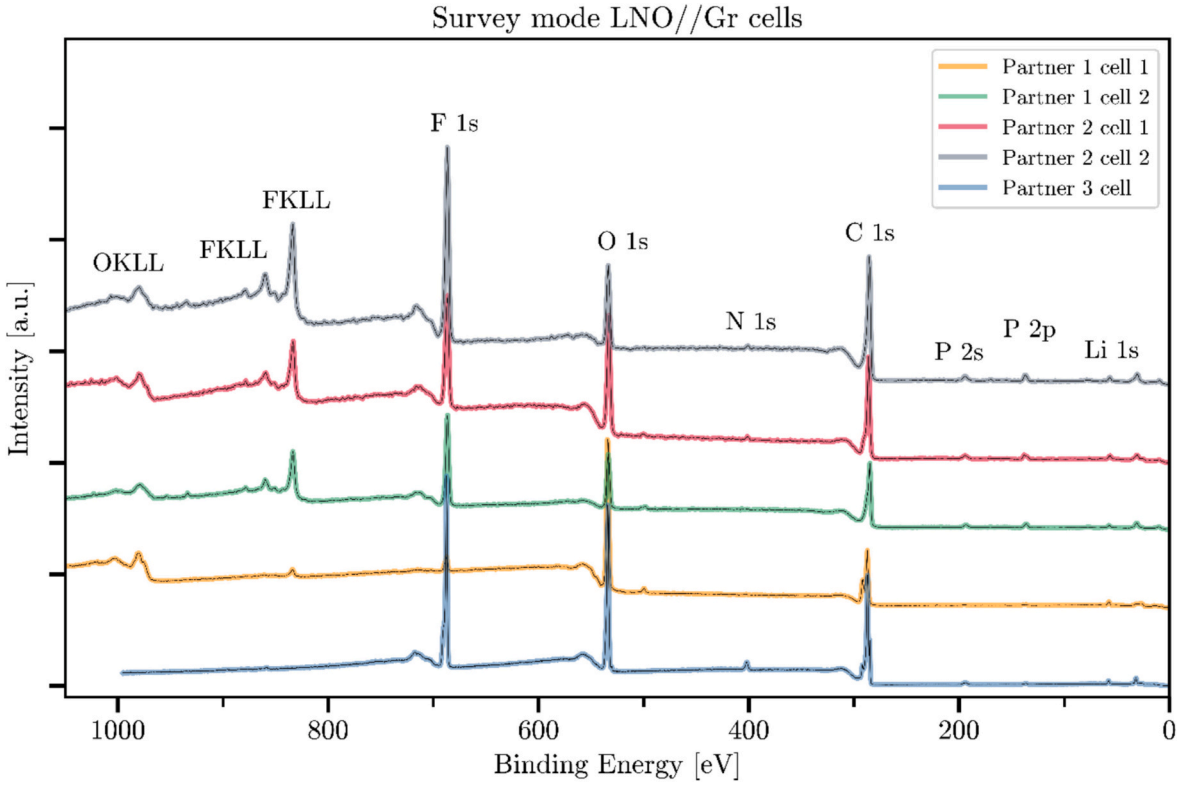

Fig. 2. Survey spectra recorded on graphite electrode cycled in LNO//Gr cell configuration during the blind reproducibility study. Spectra from Partner 1 are shown in orange and green (cells 1 and 2, respectively), from Partner 2 in red and gray, and from Partner 3 in blue (single cell). The most intense core level peaks (F 1s, O 1s, N 1s, C 1s, P 2s, P 2p and Li 1s) as well as the main Auger transitions (F KLL and O KLL) are indicated. Details of the three partners are provided in Table 1. (For interpretation of the references to colour in this figure legend, the reader is referred to the web version of this article.)

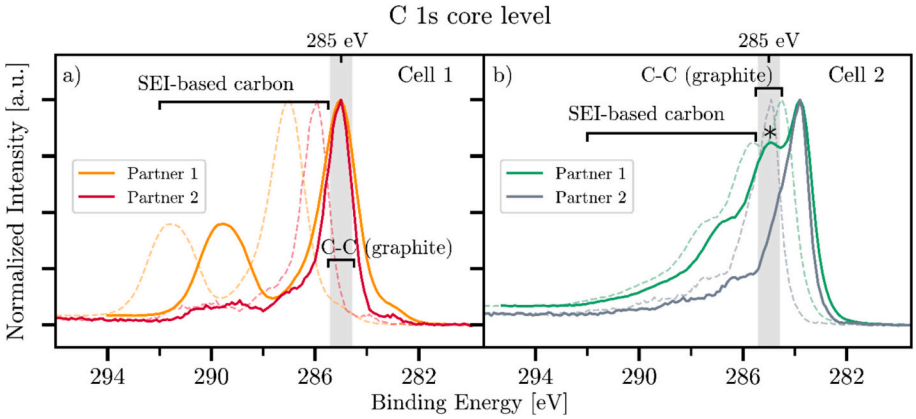

Fig. 3. Comparison of C 1s core-level spectra for graphite electrodes extracted from cell 1 and cell 2 for Partners 1 and 2, obtained during the blind reproducibility study. Line colors correspond to those used in Fig. 2. Spectra are normalized, and binding energies are calibrated (solid lines) using the aliphatic carbon peak at 285 eV, which is highlighted in gray. Dashed lines correspond to the spectra prior to calibration.

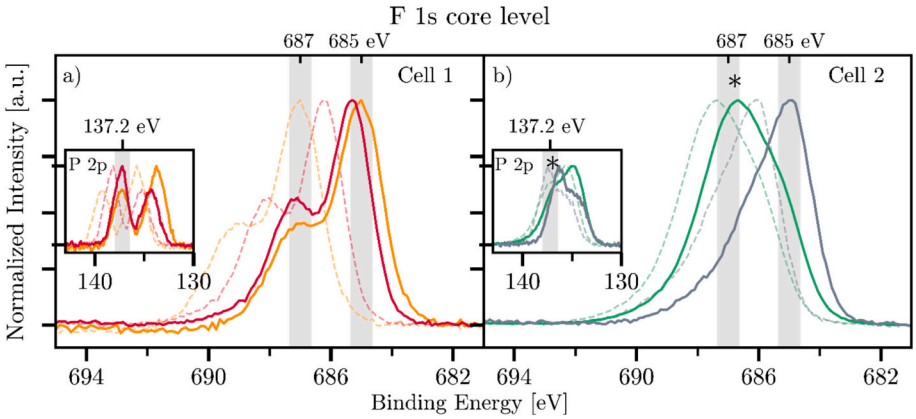

Fig. 4. Comparison of *F* 1s core-level spectra. Line colors follow the same convention as in Fig. 3. Binding energies at 685 eV and 687 eV are highlighted in gray. The insets show the P 2p core level spectra, with the binding energy at 138 eV also highlighted. The spectral region indicated by "*" in *C* 1s, *F* 1s and P 2p illustrate the artifact that can arise from inefficient surface charge neutralization; the same feature is observed in all core-level spectra.

resolution, which can affect peak fitting and data treatment. It is possible to optimize the peak broadening associated with the choice of pass energy, either by reducing it for better energy resolution, or by analyzing reference samples with the same pass energy to establish an in-lab database for peak fitting analyses.

The XPS spectra recorded on the graphite electrode from Cell 2 show different signatures compared to those obtained from Cell 1. Specifically, the positions of the carbon (Fig. 3-b) and fluorine (Fig. 4-b) peaks do not align with any known reference value or database entries. As a result, applying the same calibration procedure used for Cell 1 does not result in consistent alignment of the C 1s and F 1s peak positions. To ensure meaningful comparison across datasets, we performed an independent energy calibration for the Cell 2 spectra. In this approach, we aligned distinct peaks in C 1s and F 1s to 285 eV and 685 eV, respectively. We identified one combination for this, where the second-highest peak in C 1s set to 285 eV. This calibration was corroborated with the O 1s core level, which exhibits a unique peak at 532 eV.

Despite the differences in absolute peak positions, the shape of the spectra obtained by both laboratories for cells 1 and 2 are different, indicating variability in surface composition of the SEI. The mismatch between peak position and referenced data from the literature is attributed to a differential charging effect, a signature of a heterogenous SEI surface chemical composition and distribution. In this case, the charging effect manifests as opposite shifts in core-binding energies and the emergence of additional peaks at higher binding energies in all spectra (marked with asterisks in C 1s, F 1s and P 2p peaks (inset figure), see Fig. 3-b and Fig. 4-b). Careful consideration of this effect is necessary. It can be addressed by improving sample preparation, optimizing the contact between the electrodes and the XPS sample holder, or by optimizing charge neutralization during XPS acquisition [45].

Fig. 4-a and b reveal the presence of two F 1s peaks: one related to LiF at 685 eV and a second peak at 687 eV assigned to salt residues remaining at the surface of the electrodes after the washing process. This assignment is supported by the presence of a P 2p peak around 138 eV, indicative of $LiPF_6$ residual salt (see inserts in Fig. 4).

Overall, the blind reproducibility study demonstrates the importance of standardizing both experimental and analytical protocols to minimize potential sources of artifacts. Such artifacts may arise at any step of the post-mortem workflow, including (i) electrode manufacturing; (ii) cell assembly and cycling; (iii) the washing procedure used after disassembly; (iv) sample preparation; (v) the choice of XPS acquisition parameters.

Despite the measures taken to protect the cells from atmospheric contamination, electrode aging within the glove box after cell disassembly remains difficult to control. This variability stems from the inherent reactivity of the electrode surfaces and the specific storage conditions used. Additionally, transferring samples between different glove boxes and analytical instruments introduces further risk of contamination, potentially altering the sample composition. The electrode surface may also undergo changes due to prolonged exposure to the X-ray beam, the vacuum environment, or the use of ionic or electronic charge neutralization methods—all of which can introduce

artifacts into the analysis [46].

The acquisition parameters, particularly the choice of pass energy, which affects the spectra broadening, can also impact the quality of both qualitative and quantitative analysis.

Building on the insights gained from this initial blind reproducibility workflow, we established an optimized protocol aimed at minimizing sources of artifacts in post-mortem XPS analysis. The main sources of variability were identified in four critical stages: (1) cell assembly, (2) cycling protocols, (3) cell disassembly, electrode washing, sample preparation, and transport, and (4) XPS data acquisition parameters and practices. These stages are outlined in the top panels of Fig. 1 (steps 1 to 5). The knowledge gained from analyzing inconsistencies and challenges in the blind study enabled us to define a structured workflow, with revised guidelines and precautions tailored to each step. These guidelines were then put into practice in the standardized workflow, ensuring greater reproducibility, improved data quality, and a more robust characterization process.

3.2. *Inter-laboratory standardized workflow with round-robin data analysis*

In the second workflow, a round-robin data analysis was conducted using XPS datasets measured by a single laboratory, Partner 1. Table 2 lists the specifications of the data acquisition parameters. The datasets consist of XPS spectra acquired on graphite electrodes cycled until 80% state-of-health (SoH) using two different electrolytes: LP57 with and without LiTDI-based electrolyte.

The round-robin analysis involved eight early-career researchers with varying levels of expertise in battery chemistry and XPS characterization. Table 3 summarizes their profiles, detailing individual backgrounds and self-reported levels of expertise in both battery chemistry and XPS. Each participant received two sets of XPS spectra measured by Partner 1, one for each type of electrolyte, containing spectra of F 1s, C 1s, N 1s, O 1s, P 2p and Li 1s core-levels.

The primary goal of XPS data analysis in this context was to determine the chemical composition of the SEI formed at the surface of the cycled graphite electrode, and how it varies with electrolyte composition. By performing qualitative and quantitative analysis, it is possible to identify and quantify the chemical species on the surface of graphite electrodes post-cycling. This process involves XPS spectra processing using iterative mathematical operations, such as spectra calibration, background subtraction and peak fitting, corresponding to step 6 in Fig. 1.

To evaluate the robustness and variability of XPS interpretation practices, the round-robin analysis was conducted blindly, i.e. participants were given no specific guidance and were free to apply their own analysis procedures. Prior to this exercise, all participants we given indications on general XPS practices for peak fitting and training on the software used for data treatment. This approach enabled us to assess how different analytical choices impact the outcome, especially when made by users with varying levels of experience. To compare the results obtained by the participants, we focus on key analytical parameters such as the choice of the background subtraction method, the distribution function used for peak fitting, and the treatment of peak area and stoichiometry. Almost all participants employed a Shirley-type background [47], which is the most common step-shaped background employed when analyzing C 1s, F 1s, O 1s, P 2p and Li 1s spectra in the literature. A linear background function was also used by two participants. For peak fitting, half of the participants used a pseudo-Voigt function, while the other half opted for an asymmetry Lorentzian function available in CasaXPS peak fitting software. In this case the asymmetric Lorentzian function was used in peak fitting to describe spectral lines that are not perfectly symmetrical, unlike a standard Lorentzian or pseudo-Voigt function. It modifies a standard Lorentzian by incorporating parameters that introduce asymmetry, such as convolution with a Gaussian function, or a mixing parameter in a combined Lorentzian function. The specific fitting parameters used by each participant are reported in Table 3.

This diversity in analytical approaches highlights the range of methodologies currently applied in the field and underscores the importance of establishing clearer guidelines. The findings from this exercise offer valuable insights into how user-dependent variability can be mitigated and contribute to the refinement of standardized practices for XPS data analysis.

a. **Result variability from peak fitting**

To illustrate the disparity in peak fitting between participants, we show the *F* 1s spectrum fit as an example in Fig. 5, and in Fig. 6 the fit for the F 1s, O 1s, C 1s, Li 1s, P 2p, N 1s and S 2p core-level spectra from Participant F, an expert in XPS and battery chemistry.

Fig. 5 shows that the *F* 1s spectrum recorded at the surface of a graphite electrode cycled without LiTDI exhibits two peaks centered at 685 and 687 eV, assigned to LiF and $LiPF_yO_z$ groups, respectively. All participants, irrespective of their scientific background, fitted the spectrum using these two distinct peaks. In this case, peak fitting relies solely on a mathematical approach to assess the contributions of LiF and $LiPF_yO_z$. Variations in analysis methodologies arise from the choice of fitting functions by each participant. Some participants opted to use a linear background function instead of a Shirley background, or chose an asymmetric peak instead of the pseudo-Voigt functions for peak fitting. However, these different choices did not alter the final quantitative and qualitative interpretation in this case. This presents an example where the selection of mathematical functions does not affect the result, as the spectrum is symmetrical and the separation between peaks is not ambiguous due spectrum asymmetry or broadening.

In the case of the *F* 1s spectrum recorded at the surface of a graphite electrode cycled with the LiTDI additive, the component at 687 eV shows an asymmetry and broadening towards lower binding energy. This is indicative of both -CF_3 related group in LiTDI and phosphates

Table 3
The table presents participant information for the round-robin exercise. Column 1 and 2 indicate participants' knowledge of the XPS technique and battery chemistry, rated as 1 for low, 2 for medium and 3 for high based on individual assessments. Column 3 details the field of expertise. Columns 4 and 5 list the functions used for background and peak fitting, respectively. Participants B and C represent groups of two individuals.

	Knowledge on XPS	Knowledge on battery chemistry	Field of expertise	Background function	Fitting function
Participant A	1	1	Data/ physics	Linear	Pseudo-Voigt (product)
Participant B	1	3	Solid state chemistry	Shirley	Lorenztian Asymmetrical
	1	2	Material science		
Participant C	3	2	Surface science	Shirley	Pseudo-Voigt (sum)
	2	2	Battery		
Participant D	2	3	Battery	Shirley/Linear	Lorenztian Asymmetrical
Participant E	3	3	Surface science	Shirley	Pseudo-Voigt (product)
Participant F	3	3	Solid state physics	Shirley	Pseudo-Voigt (product)

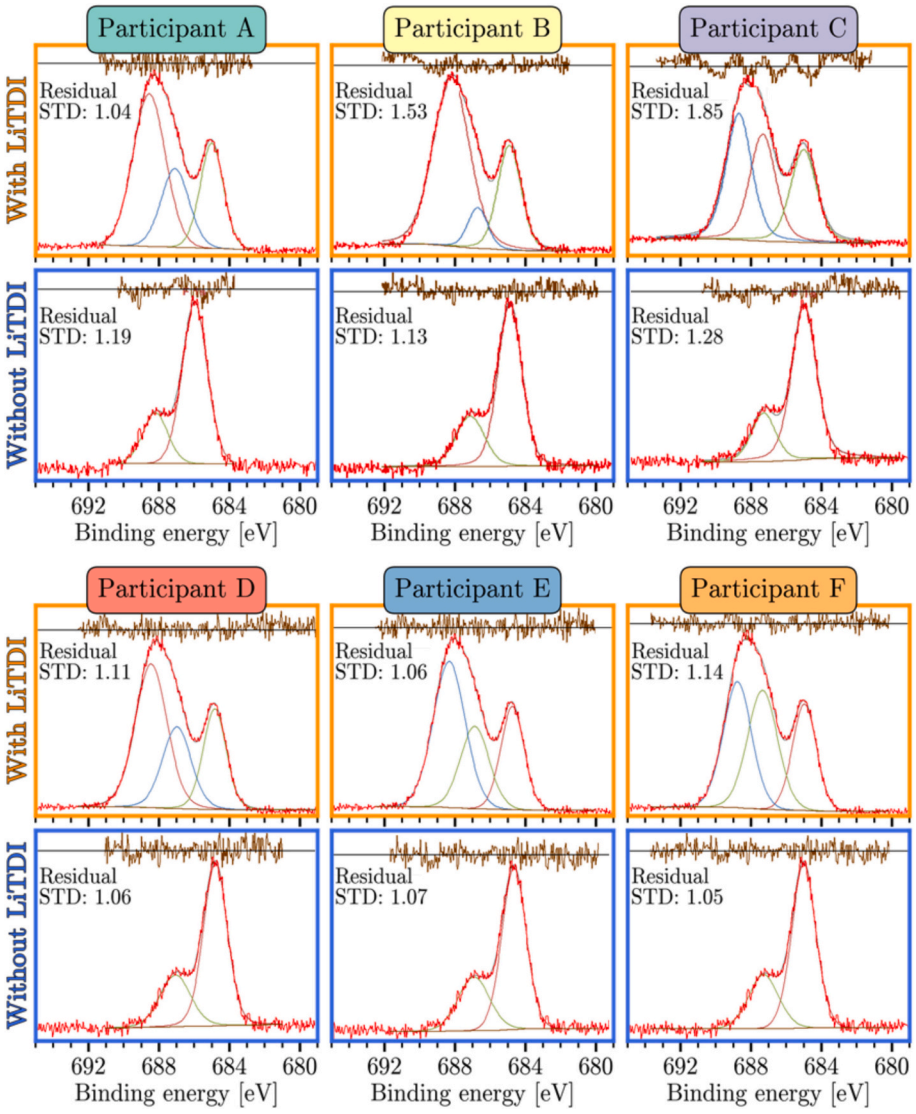

Fig. 5. F 1s core-level spectra from the round-robin analysis performed by six participants. For each participant, spectra acquired from graphite electrodes with LiTDI-based electrolyte (top row, orange boxes) and without additive (bottom row, blue boxes) are shown. Each spectrum includes the background subtraction, fitted individual peak components, and the residual between experimental data and the fit. All spectra are presented in arbitrary unit. Standard Deviation (STD) is reported on each figure to evaluate the peak fitting variability. (For interpretation of the references to colour in this figure legend, the reader is referred to the web version of this article.)

from $LiPF_6$ decomposition. To account for this peak asymmetry, all participants included a third component. However, differences in peak parameters were observed, demonstrating that mathematical considerations alone are insufficient to describe the experimental data.

Participants with expertise in both battery chemistry and XPS (e.g., E and F) considered stoichiometric aspects by combining peak ratio from the $LiPF_yO_z$ contribution in the P 2p (peak at 136 eV) spectrum and the -CF_3 contribution in the C 1s (peak at 293 eV) spectrum (see Fig. 6). Therefore, the most accurate fit in this case involves simultaneous consideration of F 1s, P 2p and C 1s core level peaks, taking into account peak position, stoichiometry ratio and full width at half-maximum (FWHM) values.

Optimal XPS analysis is tightly connected to the electrochemical process and the potential electrochemical reaction pathways. Specifically, the *F* 1s peak serves as signature of by-products resulting from salt or additive degradation, as suggested by possible chemical and/or electrochemical reactions [6,48–54]:

$$LiPF_6 \rightarrow PF_5 + LiF$$

$$PF_5 + H_2O \rightarrow 2HF + POF_3$$

$$2HF + 2Li^+ + 2e^- \rightarrow 2LiF + H_2$$

$$LiPF_6 + Li_2CO_3 \rightarrow 3LiF + POF_3 + CO_2$$

$$PF_5 + Li_2CO_3 \rightarrow 2LiF + POF_3 + CO_2$$

The presence of *F* 1s peaks at 685 and 687 eV, along with P 2p peaks at 133 and 136 eV, are the signatures of the by-products resulting from the aforementioned reaction paths.

As LiTDI can also be subjected to a decomposition during cycling to form LiF and CF_3 [55,56], this should be considered when the F 1s peak is considered. The presence of F 1s peak at 685 and 689 eV, along with C 1s peak at 293 eV related to -CF_3 species, could highlight the decomposition of LiTDI during cycle.

This underscores the importance of incorporating chemistry-based knowledge to refine purely mathematical spectral peak fitting.

b. Statistical analysis of peak fitting and discussion

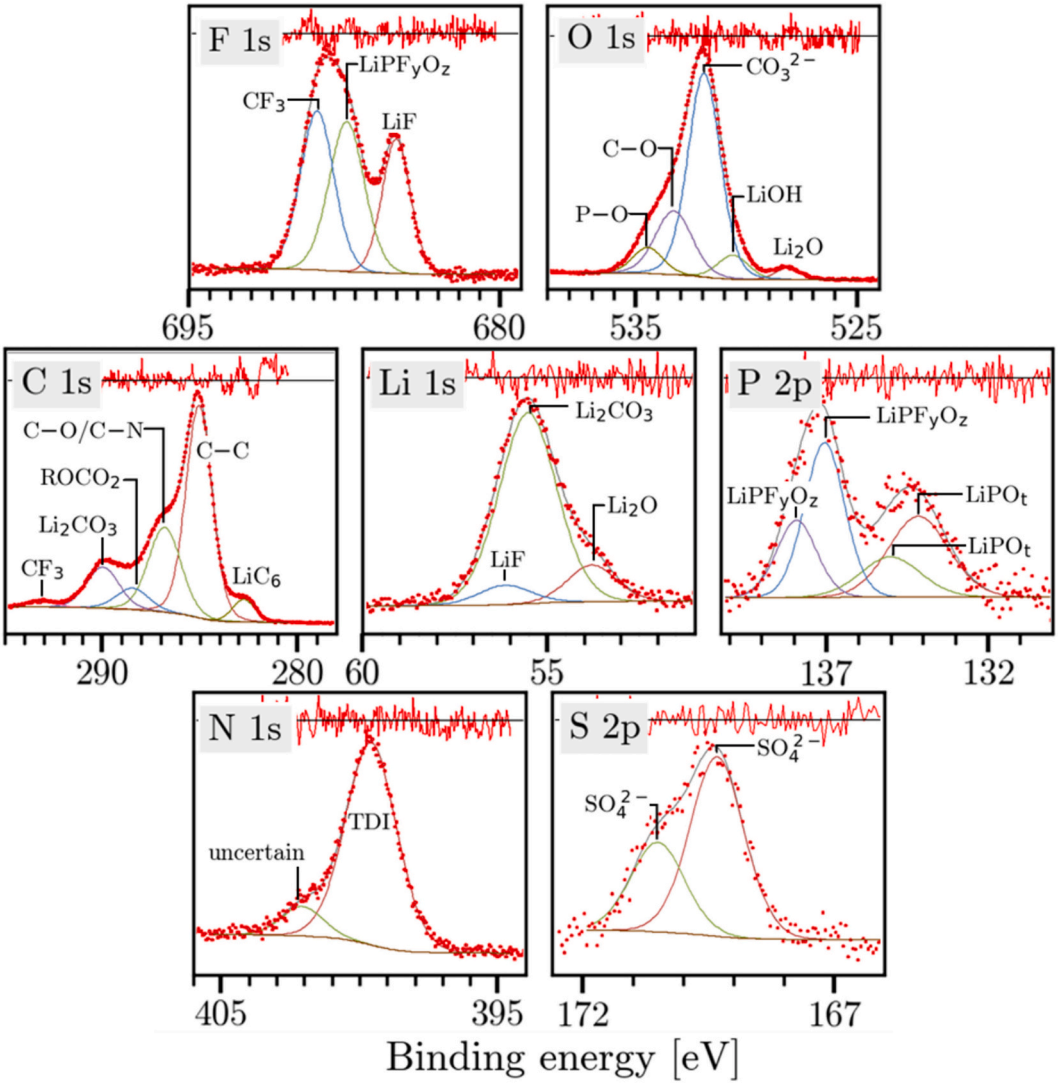

Fig. 6. Fitted XPS spectra for the sample cycled with LiTDI-based electrolyte. Top row: F 1s (left) and O 1s (right); middle row: C 1s (left), Li 1s (center), and P 2p (right); bottom row: N 1s (left) and S 2p (right). The fitting was performed by Participant F, an expert in XPS analysis and battery chemistry. Peak assignments were guided by chemical knowledge and stoichiometric constraints. All spectra are presented in arbitrary unit.

Fig. 7 illustrates the estimated atomic percentages of main elements found at the surface of the graphite electrodes (carbon, fluorine, lithium, nitrogen, oxygen, phosphorus and sulfur) as analyzed by the participants. The Blue and orange colors represent the graphite electrodes cycled in electrolyte with and without LiTDI additive, respectively. Atomic percentages were calculated using sensitivity factors provided by the partner who performed the XPS characterization (Partner 1). All participants found similar atomic percentages for the identified species and determined comparable relative percentages for each sample.

However, they noticed differences in the SEI composition between the cycled electrodes. Specifically, the atomic concentrations of oxygen, fluorine, and lithium were higher in the electrode cycled with the additive as compared to the one cycled in the electrolyte without. We can highlight that the SEI composition is different for both electrodes, the presence of nitrogen and -CF_3 related peak in the *C* 1s spectrum, evidenced the role that LiTDI could play as an additive in the electrochemical process.

All participants estimated similar atomic concentration with minor disparities, showing that the initial level of data analysis, which does not include peak fitting, is not a major source of artifact. However, this level of data analysis is insufficient to resolve the chemical composition of the SEI. Participants were asked to provide a second level of quantification based on peak fitting analysis. This analysis estimates the SEI composition based on the relative percentage of atomic environments. Fig. 8 shows a detailed comparison of the relative atomic percentages estimations extracted from C 1s, F 1s, O 1s and Li 1s peak fitting of the spectra recorded at the surface of both electrodes.

Fig. 9. and Fig. 10 present comparisons between peak positions (top plots) and FWHM (bottom plots) based on statistical analysis of the peak fitting results performed by all participants, for the cell without and with additive, respectively. In these plots, the x-axis represents core level components, while the y-axis represents the deviation from an expected value. Deviations were compared to the most accurate peak fitting data performed by Participant F (refer to Fig. 6 for individual peak fitting). Two types of data are plotted: blue data points represent averaged values with standard deviation as error bars, while orange data points represent individual values. Averaged values were plotted when more than three participants identified the same component. Circles, squares and triangles indicate components identified by six, five and four participants, respectively.

Analyzing these plots reveals components that are challenging to quantify without a solid understanding of battery chemistry. Regarding the LiTDI-based electrolyte sample (Fig. 10), the C 1s and O 1s spectra show the largest deviation in fitting. Notably, (i) the C 1s component

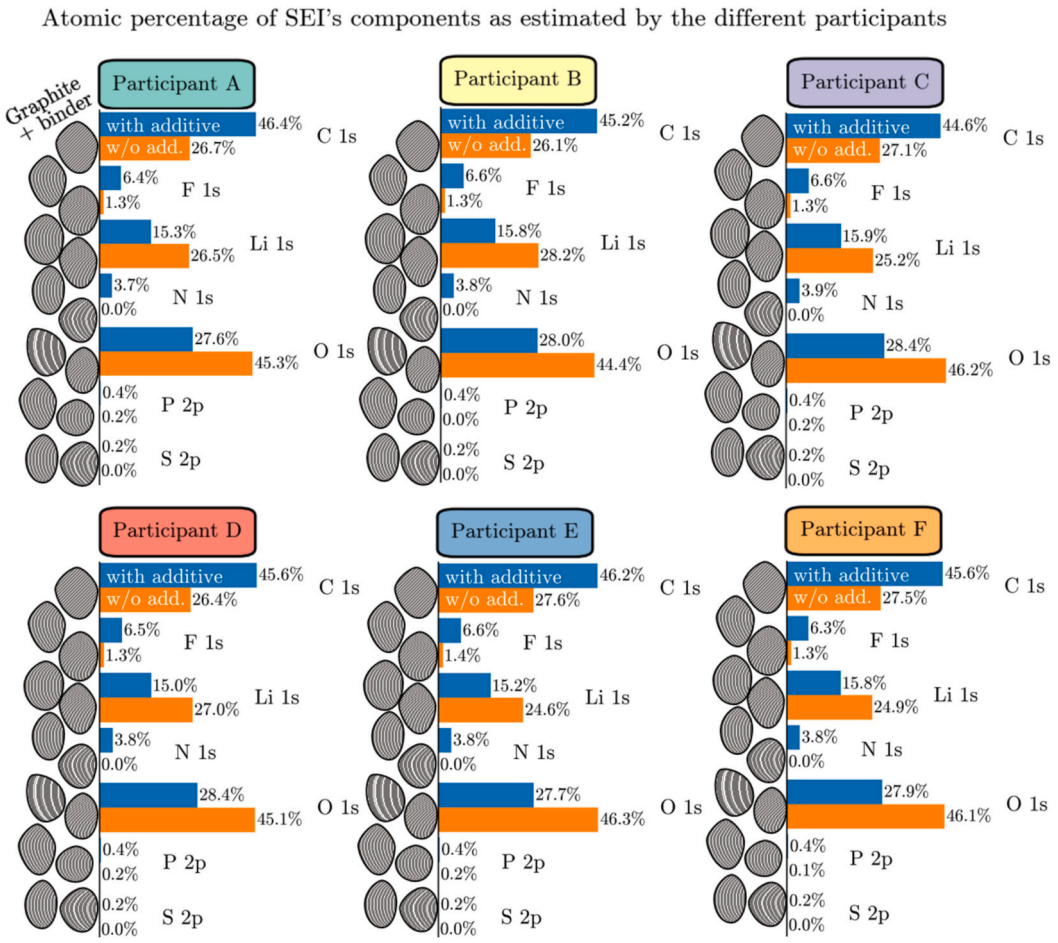

Fig. 7. Atomic percentages of SEI components (C 1s, F 1s, Li 1s, N 1s, O 1s, P 2p, and S 2p) as estimated by each participant from XPS analysis of graphite electrodes cycled in a LP57-based electrolyte. Results are shown for electrodes cycled with (blue) and without (orange) LiTDI additive. Each panel corresponds to a different participant. (For interpretation of the references to colour in this figure legend, the reader is referred to the web version of this article.)

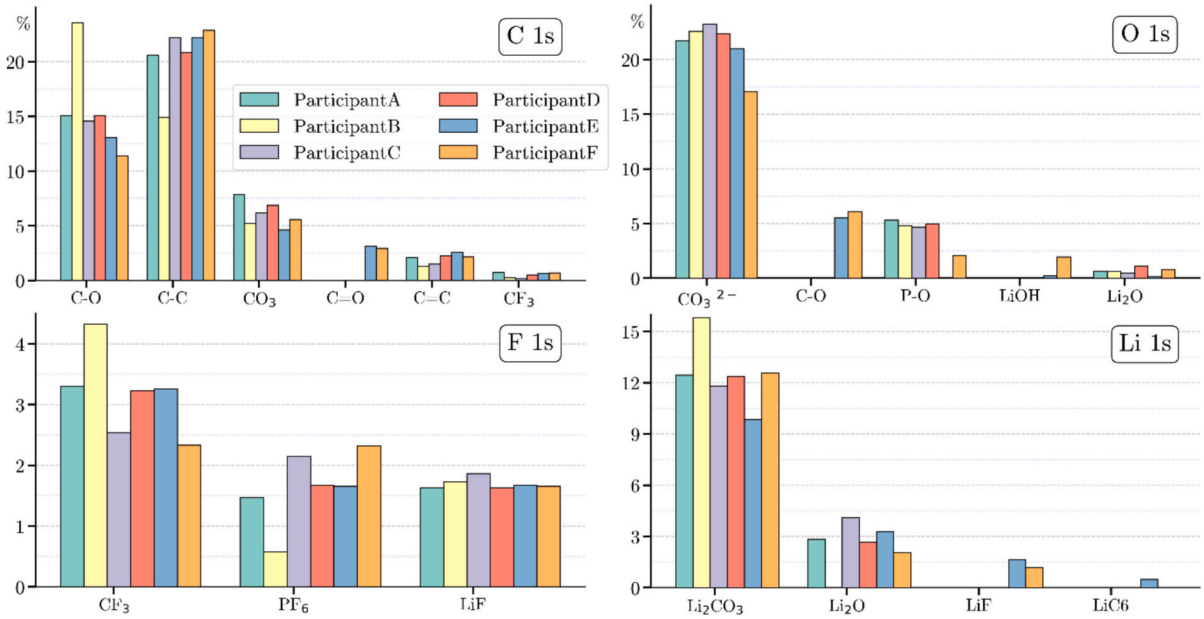

Fig. 8. Atomic percentages of fitted components from the C 1s, F 1s, O 1s, and Li 1s core levels, obtained by participants via XPS peak fitting of the spectra recorded at the surface of the electrode from the coin cell using a LiTDI-based electrolyte. Each bar represents the contribution of a specific chemical component identified within a given core level, with colors distinguishing individual participants. The data illustrate the variability in spectral interpretation and component quantification across participants.

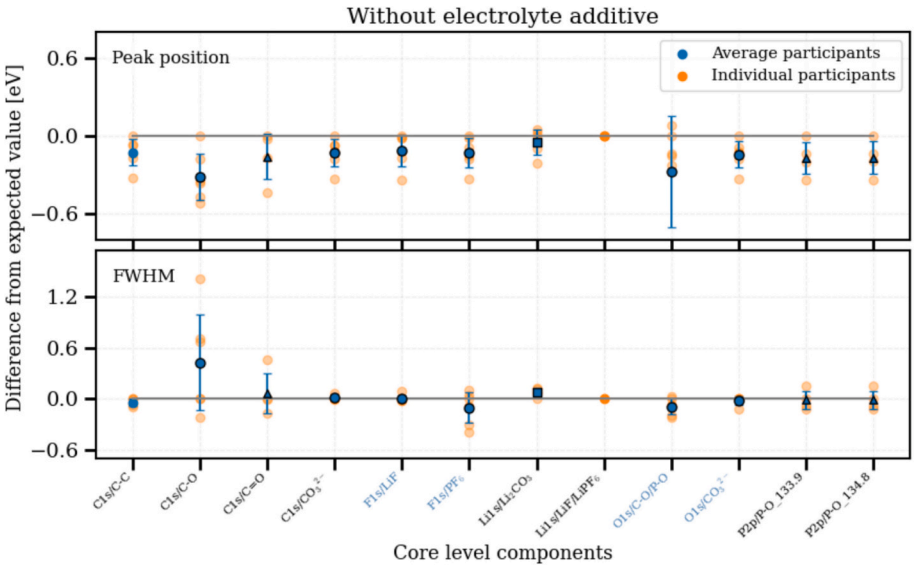

Fig. 9. Statistical assessment of fitting accuracy across participants for XPS spectra acquired from a graphite electrode cycled in a coin cell without additive. Each species-component pair is plotted along the x-axis, with deviations from the reference values shown on the y-axis for the peak position (top panel) and FWHM (bottom panel), in eV. Reference values were derived from Participant F's results. Orange markers indicate individual participant results, while blue markers represent the mean values with standard deviations as error bars. The shape of the blue markers indicates the number of contributing participants: circles for six, squares for five, and triangles for four. (For interpretation of the references to colour in this figure legend, the reader is referred to the web version of this article.)

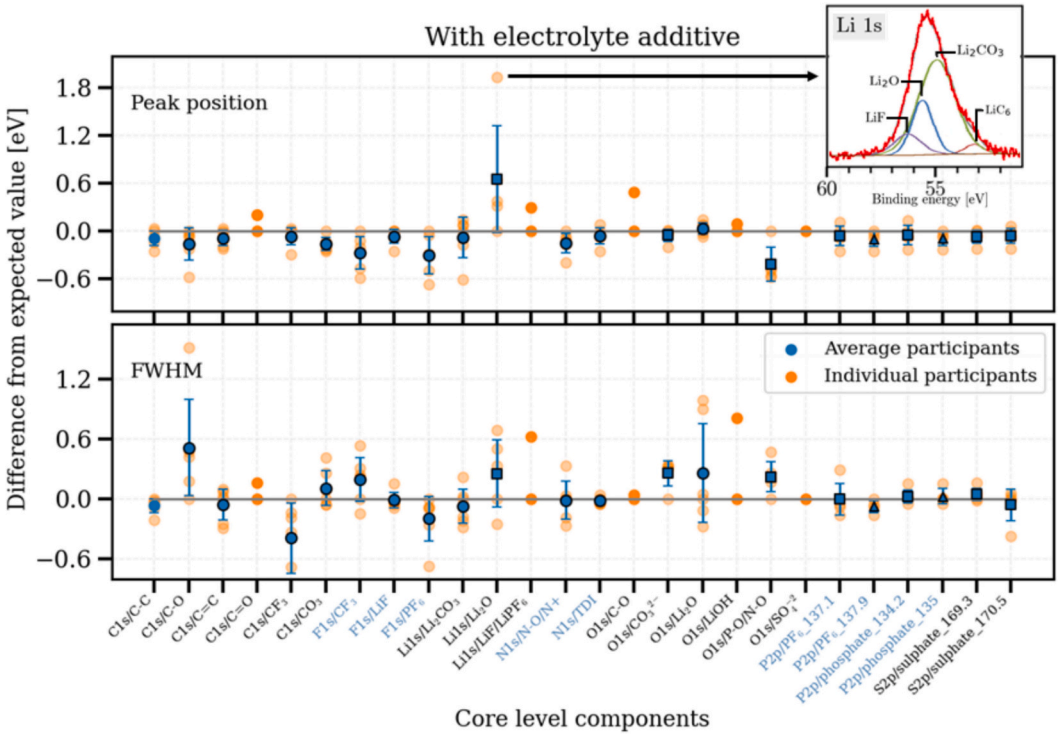

Fig. 10. Statistical assessment of fitting accuracy across participants for XPS spectra obtained from a graphite electrode cycled in a coin cell with LiTDI-based electrolyte. The axis configuration and marker conventions are consistent with Fig. 9. Deviations from Participant F's reference values are shown on the y-axis for peak position (top panel) and FWHM (bottom panel), with species–component pairs on the x-axis. Orange markers represent individual participant results, while blue markers denote mean values with standard deviations as error bars. Marker shapes indicate the number of participants contributing to each average (circle: six, square: five, triangle: four). The insert in the top panel corresponds to the Li 1s peak fitting performed by Participant E, showing Li2O and Li2CO3 identified at 1.93 eV above and 0.6 eV below the reference value, respectively. Such deviations are significantly larger than those of the other participants, who all found peak positions differing by less than one-third of these values. (For interpretation of the references to colour in this figure legend, the reader is referred to the web version of this article.)

assigned to C═O in ($ROCO_2$) at 288.5 eV was identified only by expert users; (ii) the *C* 1s component assigned to C-O/C-N related bonds exhibits a substantial mean offset value and considerable deviation in FWHM, due to its overlap with C—C and C═O, making it difficult to fit

accurately; (iii) the intensity of CF_3 component, being weak and broad, shows significant deviation in average FWHM from the expected value and standard deviation. For Li 1s and O 1s, the low binding energy shift associated to the changes in the chemical environment, manifested in their symmetrical spectra shape, renders spectral decomposition difficult. As an example, participant E fitted the Li 1s spectrum using four components, with different peak assignments. In this fit, the Li_2O and Li_2CO_3 peaks were misaligned relative to reference values: Li_2O was shifted by +1.93 eV, while Li_2CO_3 was shifted by −0.61 eV. Furthermore, an additional component attributed to LiC_6 was introduced to capture asymmetry of Li 1s at lower binding energies. This specific contribution could be linked well with the shoulder in *C* 1s peak at 283 eV (LiC_6) in Fig. 6. We noticed that participant E is the only one who proposed a peak fitting including the LiC_6 contribution. The Li 1s resulting peak fitting of participant E is presented as an inset in Fig. 10.

Regarding the *F* 1s core level, while LiF was accurately fitted with an average value very close to the expected one, the CF_3 and PF_6 ($LiPF_yO_z$) components overlap, leading to less precise individual fits.

In the P 2p core level spectrum, the low signal-to-noise ratio poses challenges in the fitting. Additional difficulties arise from the need to apply spin-orbit constraint, which requires spectrum modeling using a doublet with a fixed intensity ratio of 0.5 between the P $2p_{3/2}$ and P $2p_{1/2}$ components, and a consistent peak separation of approximately 0.8 eV. Although two overlapping doublets are expected (see Fig. 5), only three participants accounted for all key aspects—including stoichiometry, accurate peak assignment, and proper treatment of spin-orbit splitting.

Overall, the round-robin study emphasized the importance of adhering to specific protocols at each analysis stage to achieve precise peak fitting for better results interpretation. These stages include key steps, namely peak calibration, background subtraction, accurate peak assignment, and the careful selection of an appropriate peak function for fitting.

Assessments of FWHM, peak position and peak intensity further contribute to the comprehensive methodology. Cross-linking information from different peaks emerges as the most effective strategy for building a fit that provides reliable insights into the surface chemical composition.

It is essential to highlight that expertise in both XPS and battery technology is crucial for precise data analysis and interpretation. Therefore, it is evident that the development of an XPS peak fitting database would substantially enhance the accuracy of peak fitting, especially within the intricate landscape of battery chemistry. Therefore, creating such a database should be an important objective for the battery community. In addition, such curated databases are becoming increasingly valuable in the era of artificial intelligence (AI), where machine-learning approaches can be used to improve XPS peak identification and fitting. Standardized, high-quality reference datasets would not only support human experts but also enable the training of AI models that can accelerate, automate, and refine XPS data analysis in complex electrochemical systems.

4. Conclusions

Studying the evolution of the SEI in lithium-ion batteries using XPS is a powerful but complex process. As illustrated in Fig. 11, the entire process is susceptible to several sources of artifacts, beginning with cell assembly and cycling, and extending to sample transfer, washing, experiment preparation, data acquisition, data analysis and interpretation.

Cell assembly, although conducted meticulously according to specific protocols, may introduce variations in electrolyte formulations, electrode handling, and cycling conditions, potentially influencing the formation and composition of the SEI layer. The dismantling of cells post-cycling and subsequent washing steps might inadvertently leave behind residual salts or contaminants, affecting the accuracy of chemical analysis by surface sensitive technique such as XPS. During XPS data acquisition, parameters such as pass-energy and charge neutralization must be carefully adjusted to mitigate spectral enlargements and differential charging effects, which can lead to inaccuracies in peak positions, broadening and intensities. Variations in experimental setups across different laboratories, coupled with differences in expertise levels among analysts and human-induced biases in data analysis, may contribute to inconsistencies in peak fitting methodologies and data interpretation, compromising the reliability of conclusions.

To address these challenges, the battery community needs to prioritize standardized protocols and rigorous quality control. Our round-robin study highlights the critical role of inter-laboratory comparisons in validating results and promoting consistency. Such collaborative exercises are crucial for establishing consensus and best practices for every step of the post-mortem workflow, from cell dismantling to data acquisition and analysis, and should become a regular feature of community-wide research initiatives.

In addition to improving experimental protocols, we must also focus on advancing how we analyze data. A key step is the creation of standardized, community-validated XPS spectral databases. These databases would not only serve as a reference but also act as a foundation for training machine learning models for automated peak fitting and assignment. This approach will reduce subjectivity and human bias,

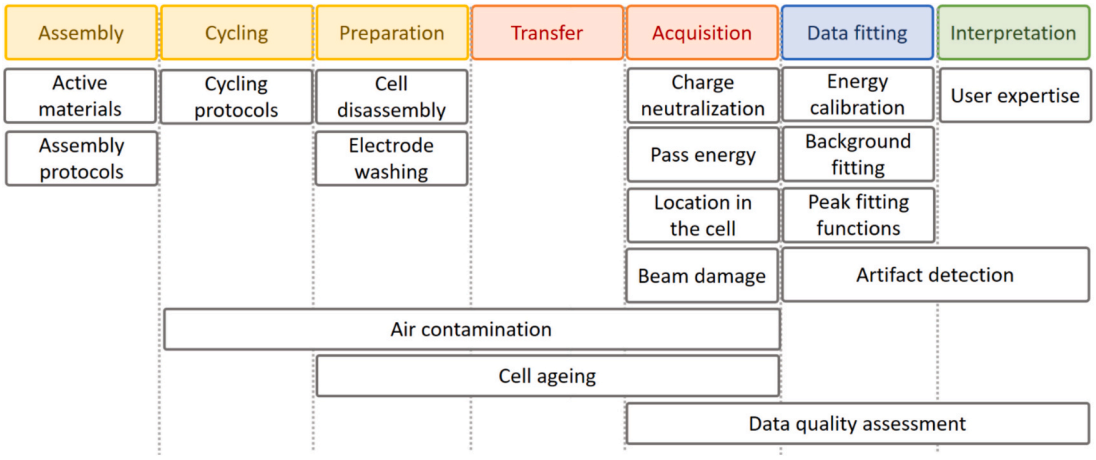

Fig. 11. Systematic identification of artifact sources affecting post-mortem XPS characterization of SEI layers in battery cells. The experimental workflow encompasses seven main stages (assembly, cycling, preparation, transfer, acquisition, data fitting, and interpretation), each associated with specific artifact sources that can impact the reliability of SEI identification and analysis.

helping to accelerate and improve the accuracy of data interpretation in the chemically complex environment of battery interfaces.

By identifying the main sources of artifacts and proposing a structured, collaborative workflow, this study provides a clear framework for more reproducible, quantitative, and predictive XPS analysis of battery interfaces. Following these recommendations is essential for improving the quality of battery research and, in turn, advancing the development of batteries with enhanced performance and longevity.

CRediT authorship contribution statement

Cinthya N. Herrera: Writing – review & editing, Writing – original draft, Visualization, Validation, Formal analysis, Data curation. **Federico Capone:** Formal analysis, Data curation. **Roberto Fantin:** Writing – review & editing, Supervision, Data curation. **François Cadiou:** Methodology, Data curation. **Nataliia Mozhzhukhina:** Validation, Methodology, Investigation. **Quentin Jacquet:** Methodology. **Jackson Flowers:** Formal analysis. **Stefan Fuchs:** Formal analysis. **Kristina Edström:** Writing – review & editing, Resources, Funding acquisition. **Andrew Naylor:** Writing – review & editing, Methodology, Investigation, Formal analysis, Data curation. **Lucía Pérez Ramírez:** Formal analysis. **Alexandre Ponrouch:** Formal analysis. **Deyana S. Tchitchekova:** Investigation, Formal analysis. **Giorgio Baraldi:** Validation, Formal analysis. **Elixabete Ayerbe:** Validation, Methodology. **Christian Wölke:** Writing – review & editing, Validation, Methodology, Investigation. **Isidora Cekic-Laskovic:** Methodology, Investigation. **Martin Winter:** Supervision. **Khawla Zrikem:** Data curation. **Shatakshi Saxena:** Data curation. **Thanh-Loan Lai:** Formal analysis. **Jean-Pascal Rueff:** Writing – review & editing, Formal analysis, Data curation. **Poul Norby:** Methodology. **Sandrine Lyonnard:** Writing – review & editing, Project administration, Methodology, Funding acquisition. **Anass Benayad:** Writing – review & editing, Writing – original draft, Visualization, Validation, Supervision, Resources, Project administration, Methodology, Investigation, Formal analysis, Data curation, Conceptualization.

Declaration of competing interest

The authors declare that they have no known competing financial interests or personal relationships that could have appeared to influence the work reported in this paper.

Acknowledgements

The authors acknowledge the support from the BIG-MAP, funded by the European Union's Horizon 2020 Research and Innovation Program under Grant Agreement No. 957189. The project is part of BATTERY 2030+, the large-scale European research initiative for inventing the sustainable batteries of the future. A.J.N and K.E acknowledge STandUP for Energy for financial support.

We gratefully acknowledge the contributions of each co-author to this research. A.B., C.N.H., F.Cadiou. and S.L. conceptualized the project, designed the workflow and coordinated the project. A.B., C.N.H. and S.L. prepared figures and wrote the manuscript; A.B., K.Z, A.N., F. Capone and J.P.R. performed XPS data acquisition and participated in the blind reproducibility tests; Q.J. and N.M. participated in the blind test; A.B., F.Capone and R.F. tutored the round-robin analysis; C.N.H., F. Cadiou, J.F., S.F., L.P.R., A.P., G.B., S.S., L.T.L. and P.N. participated in the round-robin analysis; N.M. assembled and cycled cells for the blind reproducibility tests; G.B., E.A., D.S.T, C.W. and I.C-L. assembled and cycled cells for the standard workflow. A.B. designed and realized the abstract figure. All authors contributed to the discussion of the results.

Data availability

Data will be made available on request.

References

[1] E. Peled, The electrochemical behavior of alkali and alkaline earth metals in nonaqueous battery systems—the solid electrolyte interphase model, J. Electrochem. Soc. 126 (1979) 2047–2051.
[2] M. Winter, J.O. Besenhard, M.E. Spahr, P. Novak, Insertion electrode materials for rechargeable lithium batteries, Adv. Mater. 10 (1998) 725.
[3] J. Maibach, F. Lindgren, H. Eriksson, K. Edström, M. Hahlin, Electric potential gradient at the buried Interface between lithium-ion battery electrodes and the SEI observed using photoelectron spectroscopy, J. Phys. Chem. Lett. 7 (2016) 1775–1780.
[4] J.O. Besenhard, M. Winter, J. Yang, W. Biberacher, Filming mechanism of lithium-carbon anodes in organic and inorganic electrolytes, J. Power Sources 54 (1995) 228.
[5] E. Peled, D. Golodnitsky, G. Ardel, V. Eshkenazy, The SEI model—application to lithium polymer electrolyte batteries, Electrochim. Acta 40 (1995) 2197–2204.
[6] D. Aurbach, M.D. Levi, E. Levi, A. Schechter, Failure and stabilization mechanisms of graphite electrodes, J. Phys. Chem. B 101 (1997) 2195.
[7] E. Peled, Advanced model for solid electrolyte interphase electrodes in liquid and polymer electrolytes, J. Electrochem. Soc. 144 (1997) L208.
[8] E. Peled, D. Golodnitsky, C. Menachem, D. Bar-Tow, An advanced tool for the selection of electrolyte components for rechargeable lithium batteries, J. Electrochem. Soc. 145 (1998) 3482.
[9] D. Aurbach, Review of selected electrode-solution interactions which determine the performance of Li and Li ion batteries, J. Power Sources 89 (2000) 206–218.
[10] D. Aurbach, M. Daroux, P. Faguy, E. Yeager, Identification of surface films formed on lithium in propylene carbonate solutions, J. Electrochem. Soc. 134 (1987) 1611.
[11] K. Kanamura, H. Tamura, S. Shiraishi, Z. Takehara, XPS analysis of lithium surfaces following immersion in various solvents containing $LiBF_4$, J. Electrochem. Soc. 142 (1995) 340.
[12] R. Dedryvère, L. Gireaud, S. Grugeon, S. Laruelle, J.-M. Tarascon, D. Gonbeau, Characterization of lithium alkyl carbonates by X-ray photoelectron spectroscopy: experimental and theoretical study, J. Phys. Chem. B 109 (2005) 15868–15875.
[13] L. Dettmann, L.O.S. Colbin, A.J. Naylor, Influence of battery electrode chemistry on electrolyte decomposition, Adv. Mater. Interfaces 12 (2025) 2500262.
[14] D. Atkins, E. Ayerbe, A. Benayad, F.G. Capone, E. Capria, I.E. Castelli, I. Cekic-Laskovic, R. Ciria, L. Dudy, K. Edström, M.R. Johnson, H. Li, J.M.G. Lastra, M.L. De Souza, V. Meunier, M. Morcrette, H. Reichert, P. Simon, J.-P. Rueff, J. Sottmann, W. Wenzel, A. Grimaud, Understanding battery interfaces by combined characterization and simulation approaches: challenges and perspectives, Adv. Energy Mater. 12 (2022) 2102687.
[15] T. Waldmann, A. Iturrondobeitia, M. Kasper, N. Ghanbari, F. Aguesse, E. Bekaert, L. Daniel, S. Genies, I.J. Gordon, M.W. Loble, E. de Vito, M. Wohlfahrt-Mehrens, Review—post-mortem analysis of aged lithium-ion batteries: disassembly methodology and physico-chemical analysis techniques, J. Electrochem. Soc. 163 (2016) A2149–A2164.
[16] S. Leroy, F. Blanchard, R. Dedryvère, H. Martinez, B. Carré, D. Lemordant, D. Gonbeau, Surface film formation on a graphite electrode in Li-ion batteries: AFM and XPS study, Surf. Interface Anal. 37 (2005) 773–781.
[17] R. Dedryvère, H. Martinez, S. Leroy, D. Lemordant, F. Bonhomme, P. Biensan, D. Gonbeau, Surface film formation on electrodes in a $LiCoO_2$/graphite cell: a step-by-step XPS study, J. Power Sources 174 (2007) 462–468.
[18] B. Philippe, M. Hahlin, K. Edström, T. Gustafsson, H. Siegbahn, H. Rensmo, Photoelectron spectroscopy for lithium battery interface studies, J. Electrochem. Soc. 163 (2016) A178–A191.
[19] D. Aurbach, The study of electrolyte solutions based on ethylene and diethyl carbonates for rechargeable Li batteries, J. Electrochem. Soc. 142 (1995) 2882.
[20] D. Aurbach, M. Daroux, G. McDougall, E.B. Yeager, Spectroscopic studies of lithium in an ultrahigh vacuum system, J. Electroanal. Chem. 358 (1993) 63–76.
[21] F. Kong, R. Kostecki, G. Nadeau, X. Song, K. Zaghib, K. Kinoshita, F. McLarnon, In situ studies of SEI formation, J. Power Sources 97–98 (2001) 58–66.
[22] R. Schmitz, R.A. Müller, R.W. Schmitz, C. Schreiner, M. Kunze, A. Lex-Balducci, S. Passerini, M. Winter, SEI investigations on copper electrodes after Lithium plating with Raman spectroscopy and mass spectrometry, J. Power Sources 233 (2013) 110–114.
[23] R. Bhattacharyya, B. Key, H. Chen, A.S. Best, A.F. Hollenkamp, C.P. Grey, In situ NMR observation of the formation of metallic lithium microstructures in lithium batteries, Nat. Mater. 9 (2010) 504–510.
[24] S. Chandrashekar, N.M. Trease, H.J. Chang, L.S. Du, C.P. Grey, A. Jerschow, *^{7}Li MRI of Li batteries reveals location of microstructural lithium*, Nat. Mater. 11 (2012) 311–315.
[25] L. El Ouatani, R. Dedryvère, J.-B. Ledeuil, C. Siret, P. Biensan, J. Desbrieres, D. Gonbeau, Surface film formation on a carbonaceous electrode: influence of the binder chemistry, J. Power Sources 189 (2009) 72–80.
[26] I. Källquist, R. Le Ruyet, H. Liu, R. Mogensen, M.-T. Lee, K. Edström, A.J. Naylor, Advances in studying interfacial reactions in rechargeable batteries by photoelectron spectroscopy, J. Mater. Chem. A 10 (2022) 19466–19505.
[27] S. Malmgren, K. Ciosek, M. Hahlin, T. Gustafsson, M. Gorgoi, H. Rensmo, K. Edström, Comparing anode and cathode electrode/electrolyte interface composition and morphology using soft and hard X-ray photoelectron spectroscopy, Electrochim. Acta 97 (2013) 23–32.
[28] C.P. Aiken, J. Xia, D.Y. Wang, D.A. Stevens, S. Trussler, J.R. Dahn, An apparatus for the study of in situ gas evolution in Li-ion pouch cells, J. Electrochem. Soc. 161 (2014) A1548–A1554.

[29] T. Waldmann, M. Wilka, M. Kasper, M. Fleischhammer, M. Wohlfahrt-Mehrens, Temperature dependent ageing mechanisms in lithium-ion batteries – a post-mortem study, J. Power Sources 262 (2014) 129–135.
[30] S.L. Hahn, M. Storch, R. Swaminathan, B. Obry, J. Bandlow, K.P. Birke, Quantitative validation of calendar aging models for lithium-ion batteries, J. Power Sources 400 (2018) 402–414.
[31] N.M. Vargas-Barbosa, My cell is better than yours, Nat. Nanotechnol. 19 (2024) 419–420.
[32] S. Puls, E. Nazmutdinova, F. Kalyk, et al., Benchmarking the reproducibility of all-solid-state battery cell performance, Nat. Energy 9 (2024) 1310–1320.
[33] M. Kasper, A. Leike, J. Thielmann, C. Winkler, N. Al-Zubaidi R.-Smith, F. Kienberger, Electrochemical impedance spectroscopy error analysis and round robin on dummy cells and lithium-ion-batteries, J. Power Sources 536 (2022) 231407.
[34] C. Villevieille, The challenge of studying interfaces in battery materials, Nat. Nanotechnol. 20 (2025) 2–5.
[35] J. Drnec, S. Lyonnard, Synchrotron battery characterization must be more reliable, representative and reproducible, Nat. Nanotechnol. 20 (2025) 584–587.
[36] S.P. Stier, C. Kreisbeck, H. Ihssen, M.A. Popp, J. Hauch, K. Malek, M. Reynaud, T. Goumans, J. Carlsson, I. Todorov, L. Gold, A. Räder, W. Wenzel, S.T. Bandesha, P. Jacques, F. Garcia-Moreno, O. Arcelus, P. Friederich, S. Clark, M. Maglione, A. Laukkanen, I.E. Castelli, J. Carrasco, M.C. Cabanas, H.S. Stein, O. Ozcan, D. Elbert, K. Reuter, C. Scheurer, M. Demura, S.S. Han, T. Vegge, S. Nakamae, M. Fabrizio, M. Kozdras, Materials Acceleration Platforms (MAPs): accelerating materials research and development to meet urgent societal challenges, Adv. Mater. 36 (2024) 2407791.
[37] BIG-MAP Project, Official project website, 2025. https://www.big-map.eu/. (Accessed 30 April 2025).
[38] BIG-MAP project, Deliverables repository, 2025. https://www.big-map.eu/dissemination/public-project-deliverables. (Accessed 30 April 2025).
[39] BIG-MAP project, Public deliverable D5.3: Demonstration of the capability to run coordinated multi-techniques experiments to acquire multi-scale data, and practical application to a selected chemistry, 2025.
[40] N. Fairley, V. Fernandez, M. Richard-Plouet, C. Guillot-Deudon, J. Walton, E. Smith, D. Flahaut, M. Greiner, M. Biesinger, S. Tougaard, D. Morgan, J. Baltrusaitis, Systematic and collaborative approach to problem solving using X-ray photoelectron spectroscopy, Appl. Surf. Sci. Adv. 5 (2021) 100112.
[41] L. El Ouatani, R. Dedryvère, C. Siret, P. Biensan, S. Reynaud, P. Iratçabal, D. Gonbeau, The effect of vinylene carbonate additive on surface film formation on both electrodes in Li-ion batteries, J. Electrochem. Soc. 156 (2009) A103–A113.
[42] J.F. Moulder, W.F. Stickle, P.E. Sobol, K.D. Bomben, in: J. Chastain, R.C. King Jr. (Eds.), Handbook of X-ray Photoelectron Spectroscopy, ULVAC-PHI, Inc., 1995.
[43] S. Tanuma, C.J. Powell, D.R. Penn, Calculations of electron inelastic mean free paths. II. Data for 27 elements over the 50–2000 eV range, Surf. Interface Anal. 21 (1994) 165.
[44] A.M. Andersson, K. Edström, Chemical composition and morphology of the elevated temperature SEI on graphite, J. Electrochem. Soc. 148 (2001) A1100.
[45] K.N. Wood, G. Teeter, XPS on Li-battery-related compounds: analysis of inorganic SEI phases and a methodology for charge correction, ACS Appl. Energy Mater. 1 (2018) 4493–4504.
[46] R. Fantin, A. Van Roekeghem, J.-P. Rueff, A. Benayad, Surface analysis insight note: Accounting for X-ray beam damage effects in positive electrode-electrolyte interphase investigations, Surf. Interface Anal. (2014) 1–6.
[47] M.H. Engelhard, D.R. Baer, A. Herrera-Gomez, P.M.A. Sherwood, Introductory guide to backgrounds in XPS spectra and their impact on determining peak intensities, J. Vac. Sci. Technol. A 38 (2020) 063203.
[48] D. Aurbach, H. Teller, E. Levi, Morphology/behavior relationship in reversible electrochemical Lithium insertion into graphitic materials, J. Electrochem. Soc. 149 (2002) A1255.
[49] Y. Ein-Eli, S.F. McDevitt, D. Aurbach, B. Markovsky, A. Schechter, Methyl propyl carbonate: a promising single solvent for Li-ion battery electrolytes, J. Electrochem. Soc. 144 (1997) L180.
[50] D. Aurbach, Y. Ein-Eli, The study of Li–graphite intercalation processes in several electrolyte systems using in situ X-ray diffraction, J. Electrochem. Soc. 142 (1995) 1746.
[51] O. Chusid, Y. Ein-Eli, D. Aurbach, M. Babai, Y. Carmeli, Electrochemical and spectroscopic studies of carbon electrodes in lithium battery electrolyte systems, J. Power Sources 43–44 (1993) 47.
[52] D. Aurbach, Y. Ein-Eli, O. Chusid, Y. Carmeli, M. Babai, H. Yamin, The correlation between the surface chemistry and the performance of Li–carbon intercalation anodes for rechargeable "rocking-chair" type batteries, J. Electrochem. Soc. 141 (1994) 603.
[53] A.N. Dey, B.P. Sullivan, The electrochemical decomposition of propylene carbonate on graphite, J. Electrochem. Soc. 117 (1970) 222.
[54] D. Bar-Tow, E. Peled, L. Burstein, A study of highly oriented pyrolytic graphite as a model for the graphite anode in Li-ion batteries, J. Electrochem. Soc. 146 (1999) 824.
[55] F. Lindgren, C. Xu, L. Niedzicki, M. Marcinek, T. Gustafsson, F. Björefors, K. Edström, R. Younesi, SEI formation and interfacial stability of a Si electrode in a LiTDI-salt based electrolyte with FEC and VC additives for Li-ion batteries, ACS Appl. Mater. Interfaces 8 (2016) 15758–15766, https://doi.org/10.1021/acsami.6b02650.
[56] F. Lindgren, C. Xu, J. Maibach, A.M. Andersson, M. Marcinek, L. Niedzicki, T. Gustafsson, F. Bjorefors, K.A. Edstroom, A hard X-ray photoelectron spectroscopy study on the solid electrolyte interphase of a Lithium 4,5-Dicyano-2-24 (Trifluoromethyl) Imidazolide based electrolyte for Si-electrodes, J. Power Sources 301 (2016) 105–112.